ACS APPLIED MATERIALS & INTERFACES

www.acsami.org

Research Article

Enhancing the Conductivity of Laser-Induced Graphene via a Facile High-Crystallinity-Riveting Method for Multifunctional Applications

Pengfei Chen,[⊥] Zikai Li,[⊥] Yifan Chang, Xinrui Yang, Shuaihua Jiang, Wei Qian, Xun Li, Hao Yuan, Zhe Wang,* Zuhao Shi,* and Daping He*

Cite This: *ACS Appl. Mater. Interfaces* 2025, 17, 64771−64782

Read Online

ACCESS | Metrics & More | Article Recommendations | Supporting Information

ABSTRACT: Laser-induced graphene (LIG) technology has streamlined the fabrication of patterned graphene for electronics. However, the laser-induced ultrafast kinetics result in the formation of amorphous structures and high electrical resistivity, limiting its applicability in high-performance devices. Herein, we report a facile strategy of expanding interline spacing in LIG line-to-surface growth for constructing high-crystallinity-riveted surface architectures with significantly enhanced electrical conductivity. This approach enables scalable fabrication of highly conductive LIG (3,290 S m^{-1}) under ambient conditions. Compared with doping and defect-healing strategies, this in situ optimization requires no additional reagents or high-temperature treatment and enables single-step patterned fabrication. Crucially, we first identify a heterogeneous structure along the vertical scanning direction in LIG lines, comprising defect-enriched, highly crystallized, and amorphous carbon phases. Combined experimental and theoretical analyses reveal that the structural gradient arises from the laser-pulse-induced Gaussian temperature field and far-from-equilibrium reaction dynamics. On this basis, we design an interline spacing exceeding the laser spot diameter to form high-crystallinity-riveted surface architectures, an interval conventionally considered unsuitable for producing high-quality LIG. The optimized LIG demonstrates substantially enhanced performance in electromagnetic shielding, Joule heating, and strain sensing, highlighting its potential for multifunctional, application-tailored devices.

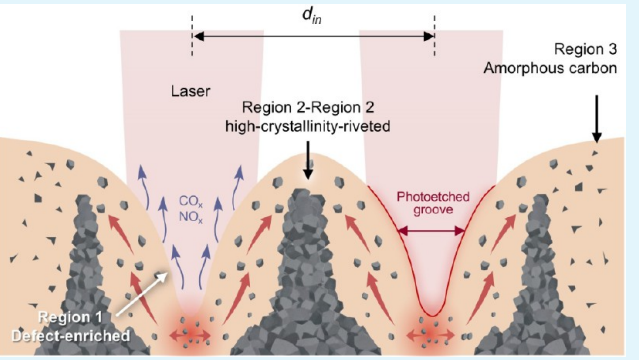

KEYWORDS: *high-crystallinity-riveted architecture, laser-induced graphene, electrical conductivity, multifunctional performance, electromagnetic shielding, strain sensor, Joule heating*

1. INTRODUCTION

Graphene has attracted significant attention due to its exceptional mechanical strength, electrical conductivity, and thermal conductivity,[1−3] motivating the development of various synthesis strategies such as chemical vapor deposition,[4−6] liquid exfoliation,[7,8] and epitaxial growth.[9,10] However, scalable fabrication under mild reaction conditions remains challenging for practical applications.

In 2014, the development of laser-induced graphene (LIG) technology marked a significant breakthrough by enabling graphene synthesis under ambient conditions.[11] This method utilizes high-energy-density laser pulses to directly convert carbonaceous precursors into patterned graphene in a single step. Consequently, LIG has been extensively studied for applications in mechanical sensors,[12−14] chemical sensors,[15−18] nanogenerators,[19−21] and supercapacitors.[22−25] Nevertheless, the ultrafast kinetics involved in laser processing results in amorphous structures, high resistivity, and diminished device performance,[26−28] necessitating strategies to enhance LIG's electrical conductivity for next-generation electronics.

Currently, high-temperature treatment has proven effective for defect healing in amorphous carbon, but it is incompatible with patterned LIG due to the extreme conditions (>1000 °C) required in vacuum or inert atmospheres (Figure S1). These conditions prevent localized heating, thus damaging both the LIG and its substrate.[29−32] To address this issue, Cheng et al.[26] reported a method using flash Joule heating through DC voltages applied selectively to LIG patterns to enable rapid defect migration within milliseconds. However, the requirement for vacuum environments and voltage control across different patterns limits scalability. Doping-based defect engineering also faces challenges. While nonmetallic and metal-oxide dopants can improve conductivity, they often result in modest improvement or introduce toxicity. For

Received: September 18, 2025
Revised: November 6, 2025
Accepted: November 6, 2025
Published: November 12, 2025

https://doi.org/10.1021/acsami.5c18748
ACS Appl. Mater. Interfaces 2025, 17, 64771−64782

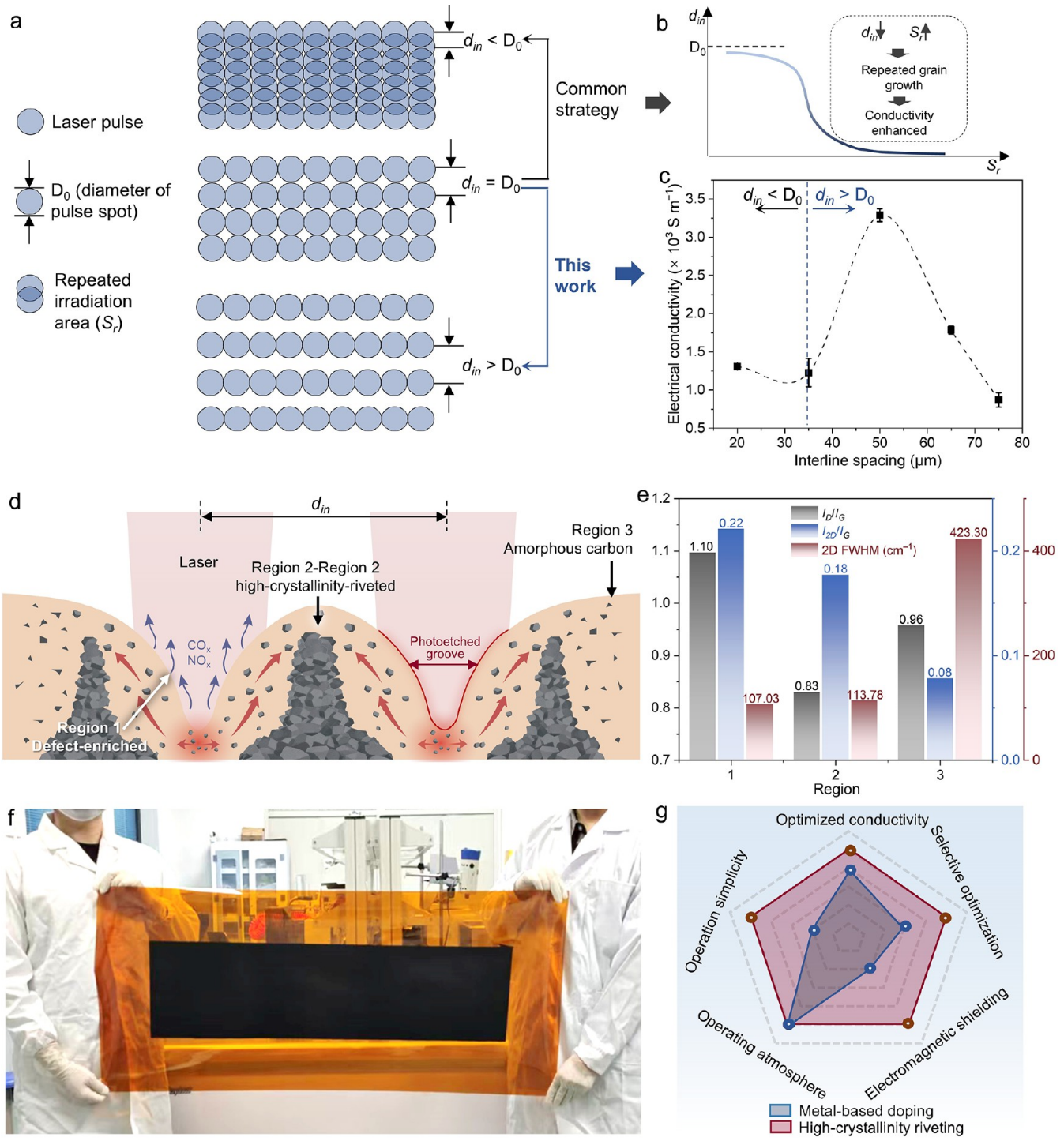

Figure 1. Design of high-crystallinity-riveting method. (a) Schematic illustrating the difference of laser scanning employed in reported works and this work. (b) Conceptual diagram showing the influence of d_{in} on S_r and electrical conductivity. (c) Electrical conductivity of LIGs fabricated under varied d_{in}. (d) Schematic of the LIG growth and HrLIG surface architecture. (e) Raman analysis at Regions 1−3, showing variations in I_D/I_G, I_{2D}/I_G, and 2D fwhm. (f) Photograph of fabricated large-area LIG film. (g) Radar chart comparing the comprehensive performance of high-crystallinity-riveted strategy versus metal-based doping.

example, metal-based dopants (e.g., NiCo, CuO, VO_x, Co_3O_4, and Fe_3O_4) significantly raise the density compared to pristine LIG (1.48×10^{-3} g cm^{-3}) and pose environmental risks.[33−38] Although codoping with N and B nonmetals can reduce structural defects and densify graphene networks, conductivity improvements remain limited, typically by only ~29.3% (from 959 S m^{-1} to 1,240 S m^{-1}).[39] Additionally, these approaches introduce complex processing steps and stringent conditions, undermining LIG's primary advantage of single-step fabrication under ambient conditions.

In this study, we identify, for the first time to our knowledge, a vertical structural gradient in LIG lines consisting of defect-enriched, highly crystalline, and amorphous carbon phases. Building on this discovery, we designed a high-crystallinity-

https://doi.org/10.1021/acsami.5c18748
ACS Appl. Mater. Interfaces 2025, 17, 64771−64782

riveted LIG (HrLIG) by expanding the interline spacing (d_{in} = 50 μm) during LIG's line-to-surface growth. Compared to reported works, such spacing exceeds the laser spot diameter (D_0 = 35 μm) and is conventionally recognized to be unsuitable for producing high-quality LIG, as it cannot guarantee complete pattern coverage. Surprisingly, this configuration enables a high-crystallinity-riveted architecture with greatly enhanced conductivity (3,290 S m^{-1}), more than 2.5 times that of nonoptimized LIG (1,308 S m^{-1}, d_{in} = 35 μm). Crucially, this approach exhibits in situ optimization, scalability and simplicity for LIG synthesis, requiring no additional reagents or post-treatment. Finite element and molecular dynamics simulations confirm the formation mechanism of the structural gradient. As a unique form of high-energy input, lasers produce a rapid thermal cycle of heating (40,746 K s^{-1}) and cooling (1,940 K s^{-1}) within the precursor, contributing to far-from-equilibrium reaction dynamics. Simultaneously, the Gaussian heat distribution leads to varied reactions, including ablation (high temperature), fine crystal growth (appropriate temperature), and incomplete reactions (low temperature). The resulting HrLIG exhibits superior performance, improving shielding effectiveness from 11,411 dB cm^{-1} to 12,920 dB cm^{-1}, increasing the Joule heating rate by 49.2%, and elevating the strain sensor gauge factor (GF) from 9.6 to 32.9. The method reported in this work offers a new paradigm for the facile design of highly conductive LIG for future applications in flexible and high-performance electronic devices.

2. EXPERIMENTAL SECTION

2.1. Preparation of LIG. PI films were purchased from Zhuzhou Times New Materials Technology Co., Ltd. (China). LIG was fabricated by laser scanning in a laser processing platform (Proteases S, LPKF, Germany), in which the PI films were irradiated by infrared laser with a 25 μm spot diameter. The sample height was set to 2 mm to achieve defocused laser scanning. The thickness of PI film was 150 μm. Experiments were conducted under atmospheric conditions at 26 °C and 45% relative humidity. The wavelength of the laser was 1,064 nm. Laser pulses were delivered at 200 kHz, and the scan speed was 15 mm s^{-1}.

2.2. Preparation of LIG/PDMS. Substrate transfer was adopted for preparing the LIG multiaxial strain sensor. A PDMS solution was prepared by mixing the prepolymer (part A) and its cross-linking agent (part B) (Sylgard 184, Sigma-Aldrich) according to the mass ratio of 10:1. Then, the PDMS was coated on the patterned LIG/PI and cured under vacuum at 80 °C for 1.5 h. Afterward, PI substrate was peeled off to get the PDMS/LIG sensor.

2.3. Molecular Dynamics (MD) Simulations. All molecular dynamics (MD) simulations were performed using the Large-scale Atomic/Molecular Massively Parallel Simulator (LAMMPS) package.[40] The interactions between atoms were described by the reactive force field (ReaxFF), which is capable of modeling dynamic bond breaking and formation, making it suitable for simulating high-temperature pyrolysis.[41] Specifically, the CHON-ffield.reax parameter set, developed for high-energy and combustion systems containing carbon, hydrogen, oxygen, and nitrogen, was employed for all simulations.[42]

2.4. Characterization. Surface morphology of the sample was characterized using a scanning electron microscope (JSM-7610F Plus, JEOL, Japan). Raman spectra were characterized with a Raman spectrometer (dxr3, Thermo Fisher Scientific, USA). X-ray diffraction (XRD) patterns were characterized with an X-ray diffractometer (Empyrean, PANalytical B.V., Netherlands). Transmission electron microscopy (TEM) images were obtained using a high-resolution transmission electron microscope (HRTEM, JEM-2100F, Japan). Electrical conductivity was measured along the laser-scanning direction using a 4-Point Probes Resistivity Measurement System (RTS-8, four Probes Tech, China) to eliminate the influence of contact resistance on results. A hyper-depth of field three-dimensional microscopic system (VHX-600E, Keyence, Norway) was adopted to capture high-definition images of surface topography. Electromagnetic shielding measurements were carried out in a rectangular waveguide using a vector network analyzer (N5225A, Keysight, USA). Near-field shielding performance was conducted by a measurement system in anechoic chamber. In this system, a scanning probe was employed to capture a near field signal leakage (magnetic field signal, H) from the covered shielding materials. One end of the microstrip antenna and the scanning probe was connected to the port 1 and port 2 of VNA, respectively. Mechanical tests were conducted using a mechanical testing machine (Instron-5848, Instron, USA) for applying uniaxial tensile strain, and the data was collected with a digital multimeter (Keithely-6510, Tektronix, USA). An auto-ranging DC power supply (IT 6953A, Itech Electronic, USA) was employed as power input in Joule heating tests, and Infrared images were captured using an infrared camera (ST9450, Wanchuang, China) to obtain the temperature of LIG.

3. RESULTS AND DISCUSSION

3.1. Design of High-Crystallinity-Riveting Method. Due to the pulsed nature of laser processing, $d_{in} \leq D_0$ is commonly employed in LIG fabrication to ensure the full coverage of the patterned area (Figure 1a). Under this condition, decreasing d_{in} increases the overlapping irradiated area (S_r) and results in repeated graphene growth, thereby improving electrical conductivity (Figure 1b). In this work, D_0 is 35 μm, and reducing d_{in} from 35 to 20 μm, only slightly improves conductivity from 1,228 S m^{-1} to 1,308 S m^{-1} (Figure 1c). However, increasing d_{in} to 50 μm leads to a dramatic conductivity enhancement, reaching 3,290 S m^{-1}. This improvement arises from the formation of high-crystallinity riveted LIG surface architectures (Figure 1d), which is based on our discovery of a grooved surface morphology and spatially uneven defect distribution in LIG lines: (1) upon efficiently absorbing 1064 nm infrared light, photothermal conversion induces a rapid temperature rise in the precursor, and excessive energy input results in photo-etching grooves along the laser scan path. Concurrently, lateral heat diffusion broadens the fabricated LIG line width beyond D_0. (2) In the direction perpendicular to scanning, the LIG line exhibits three distinct structural phases: defect-enriched (Region 1), highly crystalline (Region 2), and amorphous carbon (Region 3).

Raman spectroscopy was employed to investigate the defect structure within the LIG lines. As displayed in Figure S3, Regions 1 and 2 exhibit prominent D, G, and 2D peaks located at approximately 1340 cm^{-1} and 1580 cm^{-1}, and 2680 cm^{-1}, respectively, confirming the formation of LIG.[43−45] Among these, the D and G peaks correspond to the defect-activated breathing vibration mode of C sp^2 and the in-plane vibration of C sp^2 in an ordered graphene lattice, respectively, while the 2D peak is indicative of multilayer graphene structures.[46−48] These results suggest that the PI molecules in these two regions have undergone graphitization, involving C sp^3 to C sp^2 conversion. Notably, the Raman spectrum at Region 3 reveals significant differences in peak intensity and shape: the 2D peak is markedly diminished and broadened with an I_{2D}/I_G ratio of only 0.08 (Figure 1e), and both the D and G peaks are significantly broadened as well, indicating the absence of a layered graphene structure and the presence of typical amorphous carbon. We further conducted a quantitative analysis of defect density distribution across the three regions.

https://doi.org/10.1021/acsami.5c18748
ACS Appl. Mater. Interfaces 2025, 17, 64771−64782

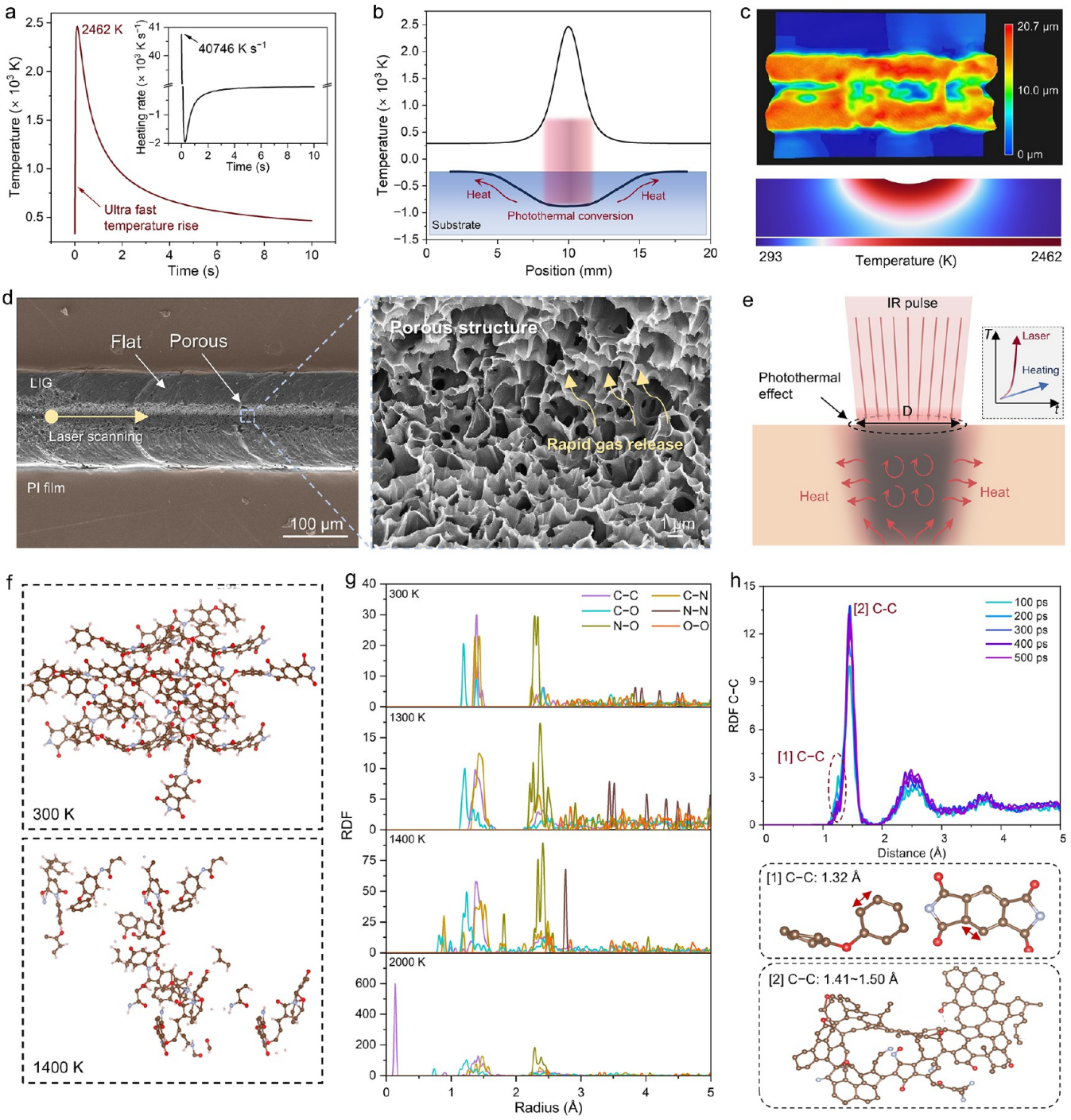

Figure 2. Formation mechanism of uneven structure in LIG lines. (a) Temperature and heating rate in different time. (b) Temperature distribution on the surface of precursor. (c) Super depth-of-field microscope images of LIG line. (d) SEM images of LIG line in different magnification. (e) Schematic illustrating function of laser pulse on precursor. (f) Simulated molecular structure of PI before and after thermal decomposition in 1,400 K. (g) RDFs of the PI molecular decomposed at various temperature. (h) RDF of C−C bond at different reaction time.

The I_D/I_G ratios at Regions 1−3 are determined to be 1.10, 0.83, and 0.96, respectively, suggesting a defect-enriched structure at Region 1 and the lowest defect density at Region 2. Meanwhile, the crystalline size along the *a*-axis (L_a) can be calculated from the I_D/I_G ratio using the following equation:

$$L_a = (2.4 \times 10^{-10}) \times \lambda_1^4 \times (I_G/I_D)$$

where λ_1 represents the Raman laser wavelength of 532 nm.[49] Compared to Regions 1 (17.5 nm) and 3 (20.1 nm), Region 2 shows the highest L_a value of 23.2 nm. In addition, Regions 1 and 2 show comparable I_{2D}/I_G ratio of 0.22 and 0.18, respectively. These results imply that the reaction conditions favor the enlargement of the crystalline domains and defect reduction in Region 2.

X-ray diffraction (XRD) reveals a dominant (002) reflection at $2\theta \approx 26°$ for all regions, with pronounced variations in peak shape (Figure S4a). Region 2 shows the most intense and sharpest (002) peak at $2\theta = 25.97°$, indicating a high degree of graphitization[11] and an interlayer spacing of ∼3.39 Å, whereas

https://doi.org/10.1021/acsami.5c18748
ACS Appl. Mater. Interfaces 2025, 17, 64771−64782

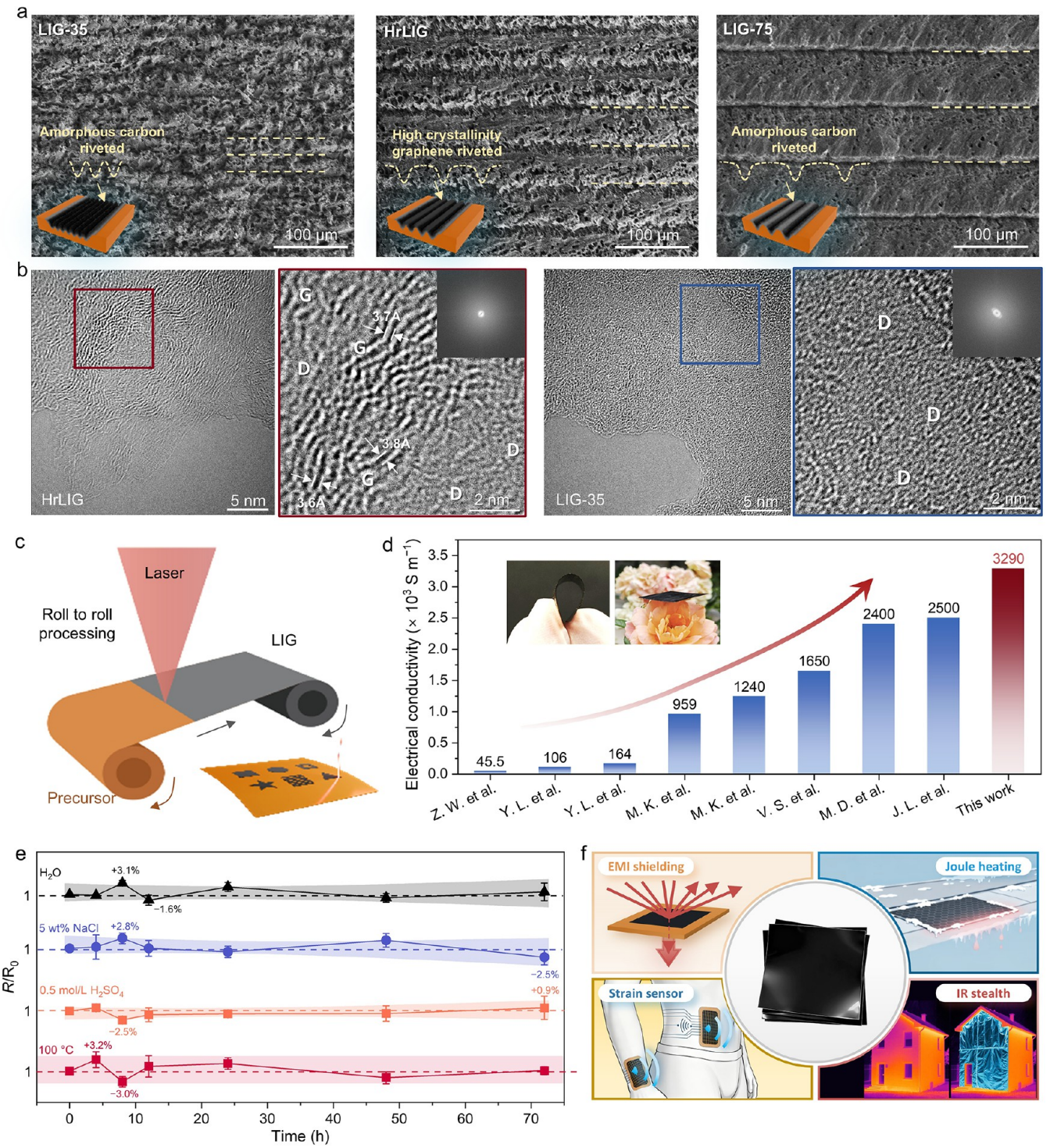

Figure 3. Characterization of HrLIG. (a) SEM images of LIG-35, HrLIG (LIG-50), and LIG-75. (b) TEM images of LIG-35 and HrLIG. (c) Characteristics of HrLIG fabrication. (d) Comparison of electrical conductivity of LIGs in reported works and this work. (e) The change rate of resistance (R/R_0) under conditions of H_2O, NaCl, H_2SO_4, and 100 °C. (f) Potential applications of HrLIG.

Region 3 features a weak, broadened peak consistent with poorly ordered amorphous carbon. The expanded interlayer spacing likely arises from defects distributed within the hexagonal graphene layers. As shown in Figure S4b, deconvolution of the diffractograms yields crystalline fractions of 50.59% (Region 1), 67.30% (Region 2), and 7.95% (Region 3), quantitatively confirming the highest crystallinity in Region 2. Selected-area electron diffraction (SAED) further corroborates these differences at the nanoscale (Figure S4c). Region 2 presents bright, well-defined rings with azimuthal arc intensifications, characteristic of polycrystalline graphene with relatively large in-plane domains. Region 1 shows weaker, more diffuse rings, while Region 3 is dominated by a broad halo, evidencing an amorphous-rich matrix with only short-range sp^2 ordering.

https://doi.org/10.1021/acsami.5c18748
ACS Appl. Mater. Interfaces 2025, 17, 64771−64782

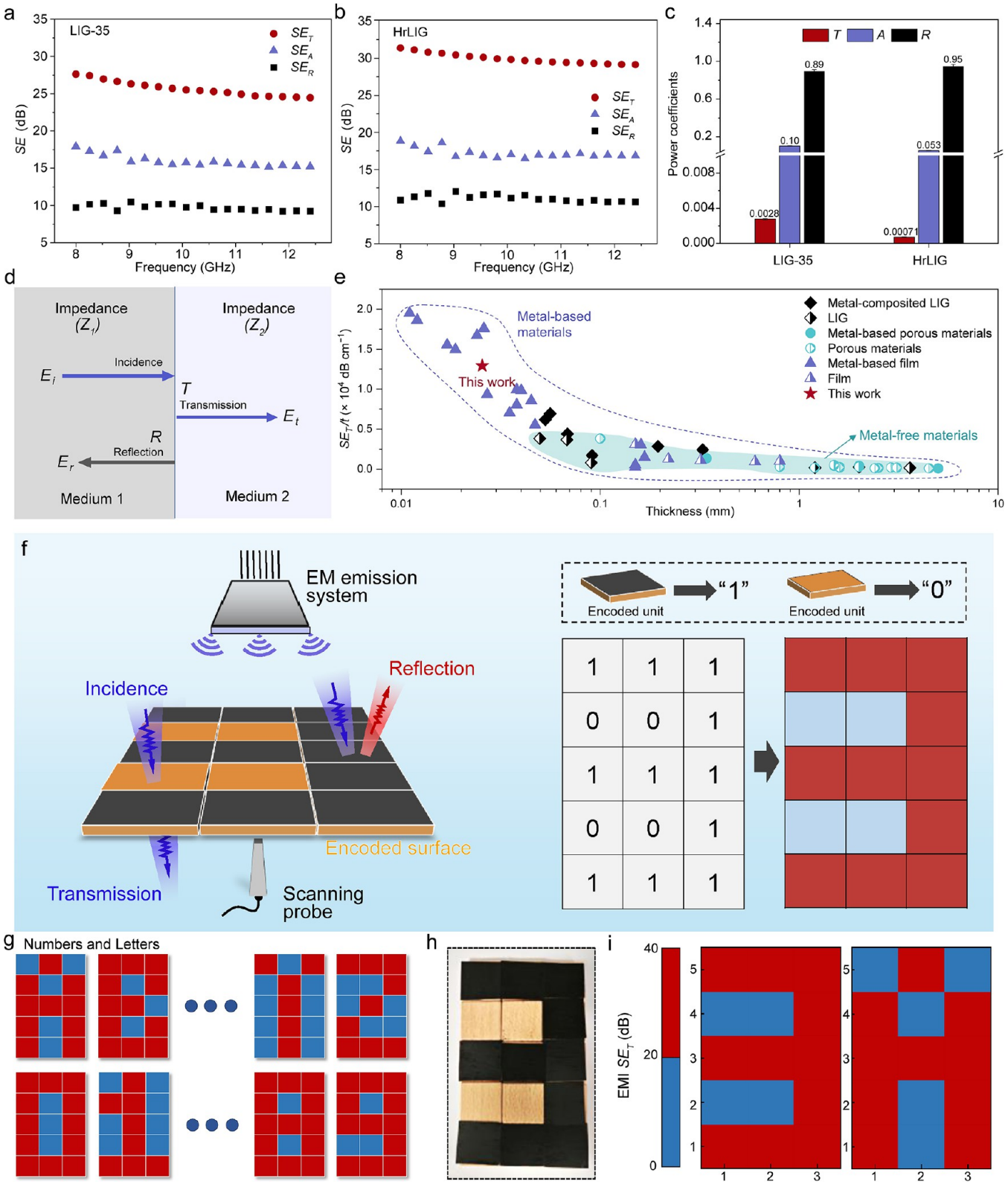

Figure 4. Application in EMI shielding. SE_T, SE_A, and SE_R of (a) LIG-35 and (b) HrLIG under wave frequency of 8−12.4 GHz. (c) *T*, *A*, and *R* of HrLIG and LIG-35 under wave frequency of 8−12.4 GHz. (d) Schematic illustration of the wave reflection and transmission at the interface. (e) Comparison of SE_T/t in reported works and this work. (f) Schematic showing the application of information encoding. (g) Schematic of encoding ability of all numbers and letters. (h) Photograph of the prepared encoded surface. (i) Electromagnetic near-field scanning test of the encoded surface.

Overall, we achieve a high-crystallinity-riveted LIG surface via a simple d_{in} tailoring strategy to enhance conductivity, challenging the conventional constraint of $d_{in} \leq D_0$. Without introducing additional reagents or complex processes, this

https://doi.org/10.1021/acsami.5c18748
ACS Appl. Mater. Interfaces 2025, 17, 64771−64782

method enables scalable, single-step fabrication of LIG under ambient conditions, with a demonstrated sample size of 1.5 × 0.5 m^2 (Figure 1f). Compared with metal-doped LIG strategies, our approach not only yields higher conductivity but also allows site-selective optimization through scan path control. The resulting high-conductivity LIG thus offers outstanding multifunctionality and broad application potential (Figure 1g).

3.2. Formation Mechanism for Heterogeneous Structure of LIG Lines. To elucidate the structural origin of the heterogeneous structure in LIG lines, a series of multiscale characterizations and simulations were performed to investigate the thermal evolution behavior of the polyimide (PI) precursor during laser irradiation. Figure 2a reveals a temporal heating profile with an extremely high peak temperature (~2,462 K) reached within milliseconds, corresponding to a heating rate exceeding 40,000 K s^{-1}. This rapid photothermal conversion contributes to far-from-equilibrium reaction dynamics,[50] where ultrafast heating likely creates a localized microvacuum environment for LIG formation, while ultrafast cooling inhibits grain growth. Additionally, a strong Gaussian-distributed temperature gradient is established across the laser spot (Figure 2b), promoting directional heat conduction. This nonuniform thermal field is further confirmed by thermal mapping and deep-field microscopy (Figure 2c), indicating that heterogeneous structures arise from spatially varying heating. Due to the excessive central temperature (~2,000 K), the center of the LIG line exhibits a photoetched groove approximately 20 μm deep. Scanning electron microscopy (SEM) imaging (Figure 2d) reveals a distinct "flat-porous" dual-region morphology, with the porous zone facilitating gas escape due to localized overheating and groove formation. Compared with conventional heating strategy, the laser-induced ultrafast temperature rise due to photothermal conversion and uneven temperature distribution, which lays the foundation for heterogeneous structural features of LIG lines (Figure 2e).

To further understand the structural evolution, molecular dynamics (MD) simulations were employed. Molecular snapshots (Figure 2f) show that at 300 K, PI chains form dense amorphous aggregates. At 1,400 K, the aggregates decompose into smaller molecular fragments, indicating significant thermal degradation. Radial distribution functions (RDFs) (Figure 2g) show that C−N bonds are preferentially broken at 1,400 K, while at 2,000 K, C−N and C−O bonds are nearly eliminated, leaving primarily C−C bonding. The evolution of C−C bonding (Figure 2h) shows sharp peaks around 1.42−1.50 Å, characteristic of C sp^2 networks, with additional peaks around 1.32 Å indicating defect sites or strained configurations.

Overall, the heterogeneous morphology of LIG originates from the interplay between rapid photothermal conversion, spatiotemporal heat gradients, and incomplete relaxation of carbon intermediates. Specifically, excessive temperatures (~2,000 K) at the center decompose PI into gaseous products and form porous and defect-enriched Region 1. In contrast, moderately high temperatures promote more complete carbonization and graphitization (Region 2), while lower temperatures (Region 3) result in the formation of amorphous carbon.

3.3. Characterization of HrLIG. Figure 1c has demonstrated the enhanced conductivity of HrLIG (LIG-50), thus SEM and transmission electron microscope (TEM) were further employed to investigate the structural features of LIG and to validate the formation of the high-crystallinity-riveted structure. As shown in Figure 3a, LIGs with different interline spacing (LIG-35, HrLIG, and LIG-75) all display a consistent stripe-like surface morphology, with increasing spacing between the groove structures reflecting the progressive increase in interline spacing. The SEM images of HrLIG reveal an interline spacing of approximately 50 μm and a moderately sized riveted region. Riveted regions that are too small or too large, as seen in LIG-35 and LIG-75 respectively, are presumed to correspond to defect-enriched or amorphous carbon-dominated surfaces. TEM analysis (Figure 3b) further reveals that the HrLIG sample exhibits a well-defined layered lattice fringe structure, characterized by prominent graphitic (002) planes with interlayer spacings of approximately 3.7 nm, indicating high crystallinity. The selected area electron diffraction (SAED) pattern displays a relatively sharp diffraction ring, consistent with turbostratic stacking of graphene layers. In contrast, LIG-35 predominantly exhibits disordered carbon regions with numerous defects, evidenced by irregular contrast and diffuse SAED patterns. These observations confirm the laser-induced crystallinity diversity and demonstrate that HrLIG achieves an optimal balance between the amorphous matrix and embedded crystalline graphene domains through a simple interline spacing adjustment strategy.

The fabrication scalability of HrLIG is schematically illustrated in Figure 3c, highlighting its compatibility with roll-to-roll laser processing and single-step patterning. Leveraging this strategy, the electrical conductivity of HrLIG reaches an impressive 3,290 S m^{-1} (Figure 3d), exceeding that of previously reported LIGs. In addition to superior conductivity, HrLIG exhibits robust environmental and thermal stability. As shown in Figure 3e, the normalized resistance (R/R_0) remains nearly unchanged (<±3.2%) after prolonged exposure (up to 72 h) to harsh conditions, including tap water, 5 wt % NaCl, 0.5 mol L^{-1} H_2SO_4, and heating at 100 °C. Such durability under corrosive, humid, and thermal environments renders HrLIG suitable for practical deployment in wearable electronics and outdoor applications. Finally, the multifunctionality of HrLIG is demonstrated through multiple conceptual use cases (Figure 3f), including electromagnetic interference (EMI) shielding, Joule heating, strain sensing, and infrared stealth. The combination of high conductivity, patternability, mechanical flexibility, and stability enables HrLIG to serve as a universal platform for next-generation electronic materials.

3.4. Application in EMI Shielding. The EMI shielding capability was systematically evaluated in the X-band frequency range (8−12.4 GHz), which is commonly used for radar detection and specialized communications.[51−54] As depicted in Figure 4a and b, HrLIG shows significantly higher total shielding effectiveness (SE_T), with values exceeding 31 dB across the measured spectrum, compared to ~26 dB for LIG-35. The average SE_T of HrLIG and LIG-35 is determined to be 31.51 and 25.67 dB, respectively (Figure S17). Furthermore, the power coefficients of transmission (T), reflection (R), and absorption (A) are calculated using the following formula:

$$T = |S_{21}|^2$$

$$R = |S_{11}|^2$$

$$A = 1 - R - T$$

https://doi.org/10.1021/acsami.5c18748
ACS Appl. Mater. Interfaces 2025, 17, 64771−64782

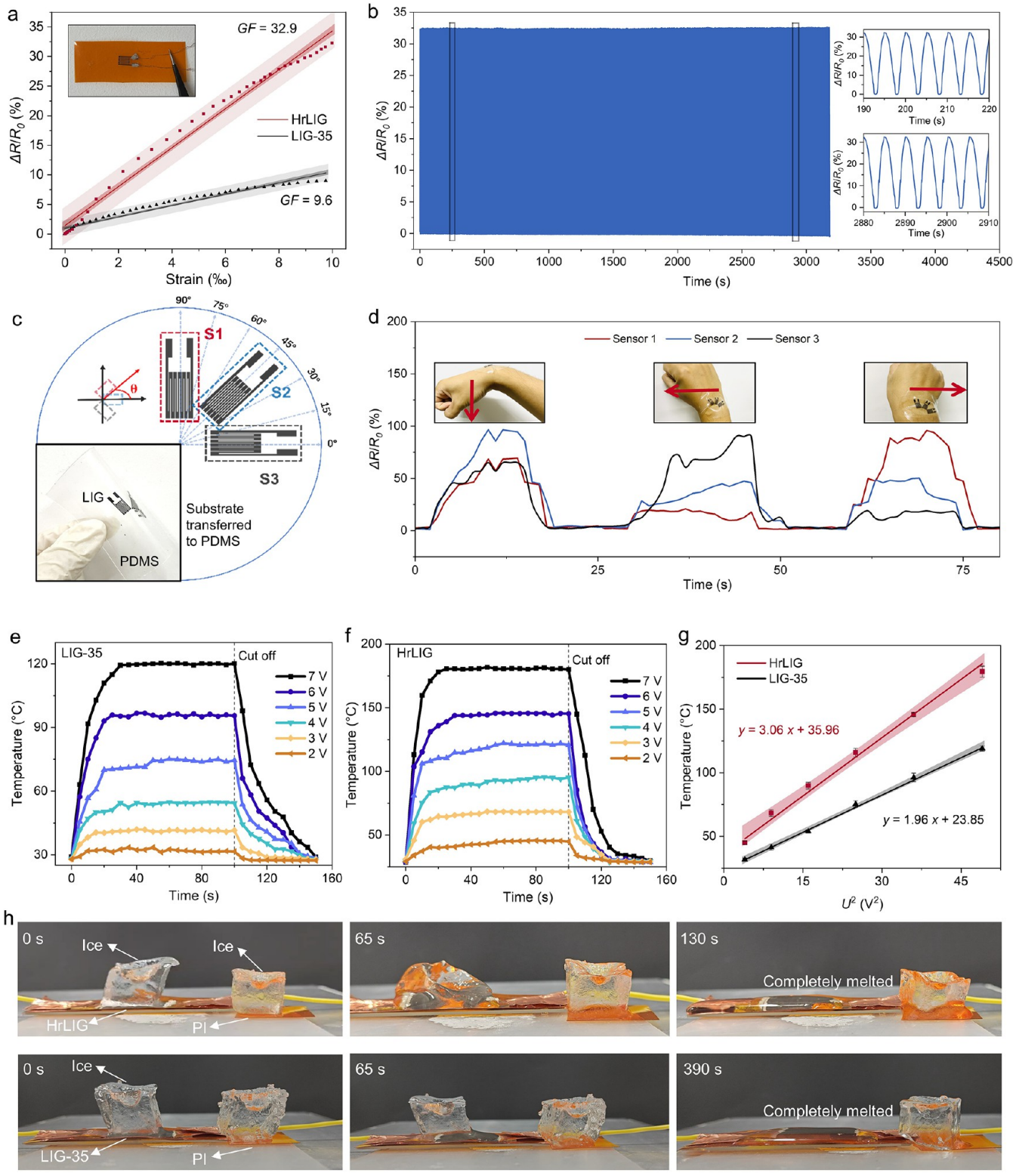

Figure 5. Applications in strain sensor and Joule heating. (a) Change of $\Delta R/R_0$ versus tensile strain for LIG-35 and HrLIG based sensor. (b) Change of $\Delta R/R_0$ versus tensile strain for HrLIG based sensor in long-term cyclic test in 3200 s. (c) Schematic and photograph of multiaxis strain sensor. (d) Change of $\Delta R/R_0$ under sequential human joint bending motions for LIG based multiaxis strain sensor. Temperature−time curves of (e) LIG-35 and (f) HrLIG under various applied voltages. (g) Temperature of LIG-35 and HrLIG at various U^2. (h) Photographs of ice melting tests on HrLIG and LIG-35 surfaces under 7 V.

where S_{21} and S_{11} were measured using a vector network analyzer. As shown in Figure 4c, HrLIG exhibits a markedly lower T coefficient (0.00071) compared to LIG-35 (0.0028), a reduced A coefficient (0.053) compared to LIG-35 (0.10), and an increased R coefficient (0.95) compared to LIG-35 (0.89).

When electromagnetic waves encounter the LIG/air interface, the reflection loss depends on the impedance mismatch

https://doi.org/10.1021/acsami.5c18748
ACS Appl. Mater. Interfaces 2025, 17, 64771−64782

between the two media (Figure 4d). The intensities of the reflected and transmitted wave from a medium with impedance Z_1 to a medium with impedance Z_2 can be calculated using the following formula:

$$E_r = \Gamma E_i = (Z_2 - Z_1)/(Z_1 + Z_2)E_i$$

$$E_t = TE_i = (2Z_2)/(Z_1 + Z_2)E_i$$

where E_i, E_r, and E_t represent the intensities of the incident, reflected, and transmitted electromagnetic waves, respectively. Thus, the higher electrical conductivity of HrLIG increases the impedance mismatch between LIG and air, resulting in enhanced reflection. Importantly, the outstanding EMI shielding effectiveness of HrLIG is achieved at minimal thickness, which is important for miniaturized shielding systems.[55,56] As presented in Figure 4e and Table S2, the average specific shielding effectiveness normalized by thickness (SE_T/t) achieves 12,359 dB cm^{-1}, positioning this work among the top-performing nonmetallic materials reported to date. This performance, coupled with the facile laser patterning and scalable processing compatibility of HrLIG, would be a significant advance toward ultrathin, lightweight, and flexible shielding components for next-generation electronic and aerospace devices.

Based on HrLIG, we developed a novel paradigm for electromagnetic information encoding. As shown in Figure 4f, electromagnetic waves from the source impinge on an encoded surface comprising a 3 × 5 array of units. A scanning probe then measured the transmitted wave intensity. Units coated with LIG are defined as "1" and those without as "0". For data encoding or encryption, each unit can be assigned a "0" or "1" and subsequently decoded or decrypted. To demonstrate practicality, we employed a simple encoding scheme (Figure 4g) in which unit arrangement directly represents letter and numeral shapes. An encoded surface representing the numeral "3" is shown in Figure 4h. After near-field scanning, the pattern was decoded as "3" and "A" (Figure 4i). In practice, the mapping between digital codes and actual information can be freely defined. This electromagnetic information encoding strategy offers application potential in secure identification, anticounterfeiting, and encrypted communication interfaces, complementing traditional visual or chip-based tagging systems.

3.5. Applications in Strain Sensor and Joule Heating.

To demonstrate the potential of HrLIG for electronics-related applications, we systematically evaluated its strain sensing and Joule heating performance. As shown in Figure 5a, a serpentine-shaped strain sensor was fabricated, and the gauge factor (GF) of HrLIG reaches an impressive value of 32.9, which is over three times higher than that of LIG-35 (GF = 9.6), indicating superior sensitivity to mechanical deformation. This enhanced resistive response is attributed to the riveted graphitic domains that not only facilitate efficient charge transport under initial strain but also induce more pronounced resistance variation due to interdomain disruption upon stretching. The durability of the HrLIG-based strain sensor was validated by long-term cyclic testing under repeated tensile loading over 3,200 s (Figure 5b), during which the normalized resistance ($\Delta R/R_0$) exhibited excellent stability and repeatability with negligible signal degradation. The inset plots confirm the sensor's responsiveness and temporal consistency in both early and late cycles, underscoring its robustness for real-world applications.

To enable integration with wearable platforms, HrLIG has been successfully transferred from the polyimide substrate to a flexible polydimethylsiloxane (PDMS) matrix (Figure S20), resulting in a conformable and skin-compatible device. Building upon this, a multiaxis strain sensor was fabricated with three orthogonally arranged HrLIG elements (Figure 5c), capable of decoding directional deformation. Furthermore, in situ monitoring of joint motions from a human subject demonstrates the sensor's capability to resolve complex biomechanical activities. As illustrated in Figure 5d, three distinct signal outputs corresponding to finger bending events are clearly distinguishable, showcasing real-time, multichannel detection of sequential and dynamic motions. The signal amplitude and temporal evolution confirm the sensor's fast response, high fidelity, and suitability for wearable electronics, human-machine interfaces, and soft robotics.

Further, the Joule heating performance was systematically investigated under varying input voltages and operational conditions. As shown in Figure 5e and f, HrLIG exhibits a rapid and stable temperature rise within seconds upon electrical stimulation. Notably, at 7 V, HrLIG achieves a peak surface temperature of 182 °C, significantly exceeding the 120 °C achieved by LIG-35 under identical conditions. This superior thermal response is a direct consequence of the markedly enhanced conductivity of HrLIG, which enables more efficient resistive heating with minimal energy loss. The heating behavior of both systems follows a quadratic relationship with respect to the square of applied voltage (U^2), in accordance with Joule's law (Figure 5g). Linear fitting reveals that HrLIG exhibits a higher temperature coefficient (slope = 3.06) compared to LIG-35 (slope = 1.96), indicating that HrLIG can achieve higher temperatures at lower power inputs, which is advantageous for energy-efficient heating systems.

In practical terms, the superior Joule heating capacity of HrLIG is vividly demonstrated in the ice-melting experiments (Figure 5h). While the ice placed on LIG-35 melts slowly with residual ice still visible after 390 s, HrLIG enables complete melting within 130 s at 7 V, indicating rapid heat accumulation and transfer to the overlying medium. This highlights its potential utility in applications such as deicing coatings, wearable thermotherapy, and antifogging devices. The long-term heating curve further confirms that the device can operate continuously at high temperatures (~180 °C) for over 500 s before power cutoff, with excellent reproducibility and negligible drift (Figure S22). Collectively, these results demonstrate that HrLIG is not only a high-performance electrical conductor but also an effective and reliable thermal actuator. Its integration into lightweight, flexible, and scalable architectures underscores its potential for next-generation intelligent heating platforms.

4. CONCLUSIONS

This work presents a facile interline spacing tailoring method to construct a high-crystallinity-riveting LIG structure, significantly increasing the electrical conductivity to 3,290 S m^{-1}. Within the LIG line, a structural gradient along the vertical scanning direction was discovered, which includes defect-enriched, highly crystalline, and amorphous carbon phases. This phenomenon is attributed to the Gaussian distribution of laser-induced heat and far-from-equilibrium reaction dynamics, in which the heating rate can reach as high as 40,746 K s^{-1}. The optimal interline spacing for achieving

https://doi.org/10.1021/acsami.5c18748
ACS Appl. Mater. Interfaces 2025, 17, 64771−64782

highly conductive LIG is demonstrated to be larger than the laser spot diameter. Based on the HrLIG architecture, enhancements in EMI shielding effectiveness, Joule heating rate, and strain sensor gauge factor are achieved, demonstrating the multifunctional potential of HrLIG for flexible and high-performance electronic applications.

■ ASSOCIATED CONTENT

Supporting Information

The Supporting Information is available free of charge at https://pubs.acs.org/doi/10.1021/acsami.5c18748.

Molecular dynamics simulations; UV−vis absorbance spectra of PI film; Raman spectra; SEM images; infrared thermograms of PI substrate during laser scanning; environmental stability tests; sheet resistance measurements; structural simulations; electromagnetic shielding test setup; comparison within linear working ranges; strain sensor resistance variation tests; photograph of the near-field scanning measurement system; Joule heating tests (PDF)

■ AUTHOR INFORMATION

Corresponding Authors

Zhe Wang − *State Key Laboratory of Advanced Technology for Materials Synthesis and Processing, Wuhan University of Technology, Wuhan 430070, China;* orcid.org/0000-0003-1412-8980; Email: wangzhe0614@whut.edu.cn

Zuhao Shi − *Hubei Engineering Research Center of Radio Frequency Microwave Technology and Application, School of Physics and Mechanics and State Key Laboratory of Silicate Materials for Architectures, Wuhan University of Technology, Wuhan 430070, China*; Email: zuhao17@whut.edu.cn

Daping He − *School of Materials Science and Engineering, Wuhan University of Technology, Wuhan 430070, China; Hubei Engineering Research Center of Radio Frequency Microwave Technology and Application, School of Physics and Mechanics and State Key Laboratory of Silicate Materials for Architectures, Wuhan University of Technology, Wuhan 430070, China;* orcid.org/0000-0002-0284-4990; Email: hedaping@whut.edu.cn

Authors

Pengfei Chen − *School of Materials Science and Engineering, Wuhan University of Technology, Wuhan 430070, China; Hubei Engineering Research Center of Radio Frequency Microwave Technology and Application, School of Physics and Mechanics and State Key Laboratory of Silicate Materials for Architectures, Wuhan University of Technology, Wuhan 430070, China;* orcid.org/0009-0000-5580-1946

Zikai Li − *School of Materials Science and Engineering, Wuhan University of Technology, Wuhan 430070, China; Hubei Engineering Research Center of Radio Frequency Microwave Technology and Application, School of Physics and Mechanics, Wuhan University of Technology, Wuhan 430070, China*

Yifan Chang − *School of Materials Science and Engineering, Wuhan University of Technology, Wuhan 430070, China; Hubei Engineering Research Center of Radio Frequency Microwave Technology and Application, School of Physics and Mechanics, Wuhan University of Technology, Wuhan 430070, China*

Xinrui Yang − *School of Materials Science and Engineering, Wuhan University of Technology, Wuhan 430070, China; Hubei Engineering Research Center of Radio Frequency Microwave Technology and Application, School of Physics and Mechanics and State Key Laboratory of Silicate Materials for Architectures, Wuhan University of Technology, Wuhan 430070, China;* orcid.org/0009-0008-8917-9831

Shuaihua Jiang − *Hubei Engineering Research Center of Radio Frequency Microwave Technology and Application, School of Physics and Mechanics and State Key Laboratory of Advanced Technology for Materials Synthesis and Processing, Wuhan University of Technology, Wuhan 430070, China*

Wei Qian − *Hubei Engineering Research Center of Radio Frequency Microwave Technology and Application, School of Physics and Mechanics and State Key Laboratory of Advanced Technology for Materials Synthesis and Processing, Wuhan University of Technology, Wuhan 430070, China*

Xun Li − *School of Materials Science and Engineering, Wuhan University of Technology, Wuhan 430070, China; Hubei Engineering Research Center of Radio Frequency Microwave Technology and Application, School of Physics and Mechanics, Wuhan University of Technology, Wuhan 430070, China*

Hao Yuan − *School of Materials Science and Engineering, Wuhan University of Technology, Wuhan 430070, China; Hubei Engineering Research Center of Radio Frequency Microwave Technology and Application, School of Physics and Mechanics, Wuhan University of Technology, Wuhan 430070, China*

Complete contact information is available at: https://pubs.acs.org/10.1021/acsami.5c18748

Author Contributions

[⊥]P.C. and Z.L. contributed equally. P.C.: writing-original draft, investigation, conceptualization, formal analysis; Z.L.: validation, investigation, data curation, formal analysis; Y.C.: validation, investigation; X.Y.: validation, data curation; S.J.: investigation, software; W.Q.: investigation; X.L.: formal analysis; H.Y.: validation; Z.W.: supervision, funding acquisition; Z.S.: supervision; D.H.: supervision, funding acquisition.

Notes

The authors declare no competing financial interest.

■ ACKNOWLEDGMENTS

This work was supported by the National Natural Science Foundation of China (22279097), the Natural Science Foundation of Hubei Province (2025AFB038, 2025AFD120), the Foundation of National Key Laboratory of Microwave Imaging Technology, the first batch of joint funding by the China Postdoctoral Science Foundation and Hubei Province (2025T015HB), and the 76th Batch of General Funding of the China Postdoctoral Science Foundation (2024M762511).

■ REFERENCES

(1) Sun, Z.; Fang, S.; Hu, Y. H. 3D graphene materials: From understanding to design and synthesis control. *Chem. Rev.* **2020**, *120* (18), 10336−10453.

(2) Novoselov, K. S.; Fal'ko, V. I.; Colombo, L.; Gellert, P. R.; Schwab, M. G.; Kim, K. A roadmap for graphene. *Nature* **2012**, *490* (7419), 192−200.

(3) Geim, A. K.; Novoselov, K. S. The rise of graphene. *Nat. Mater.* **2007**, *6* (3), 183−191.
(4) Zhang, Y.; Zhang, L.; Zhou, C. Review of chemical vapor deposition of graphene and related applications. *Acc. Chem. Res.* **2013**, *46* (10), 2329−2339.
(5) Yu, Q.; Lian, J.; Siriponglert, S.; Li, H.; Chen, Y. P.; Pei, S.-S. Graphene segregated on Ni surfaces and transferred to insulators. *Appl. Phys. Lett.* **2008**, *93* (11), 113103.
(6) Sun, J.; Rattanasawatesun, T.; Tang, P.; Bi, Z.; Pandit, S.; Lam, L.; Wasén, C.; Erlandsson, M.; Bokarewa, M.; Dong, J.; Ding, F.; Xiong, F.; Mijakovic, I. Insights into the mechanism for vertical graphene growth by plasma-enhanced chemical vapor deposition. *ACS Appl. Mater. Interfaces* **2022**, *14* (5), 7152−7160.
(7) Coleman, J. N.; Lotya, M.; O'Neill, A.; Bergin, S. D.; King, P. J.; Khan, U.; Young, K.; Gaucher, A.; De, S.; Smith, R. J.; Shvets, I. V.; Arora, S. K.; Stanton, G.; Kim, H.-Y.; Lee, K.; Kim, G. T.; Duesberg, G. S.; Hallam, T.; Boland, J. J.; Wang, J. J.; Donegan, J. F.; Grunlan, J. C.; Moriarty, G.; Shmeliov, A.; Nicholls, R. J.; Perkins, J. M.; Grieveson, E. M.; Theuwissen, K.; McComb, D. W.; Nellist, P. D.; Nicolosi, V. Two-dimensional nanosheets produced by liquid exfoliation of layered materials. *Science* **2011**, *331* (6017), 568−571.
(8) Li, Z.; Young, R. J.; Backes, C.; Zhao, W.; Zhang, X.; Zhukov, A. A.; Tillotson, E.; Conlan, A. P.; Ding, F.; Haigh, S. J.; Novoselov, K. S.; Coleman, J. N. Mechanisms of liquid-phase exfoliation for the production of graphene. *ACS Nano* **2020**, *14* (9), 10976−10985.
(9) Yang, W.; Chen, G.; Shi, Z.; Liu, C.-C.; Zhang, L.; Xie, G.; Cheng, M.; Wang, D.; Yang, R.; Shi, D.; Watanabe, K.; Taniguchi, T.; Yao, Y.; Zhang, Y.; Zhang, G. Epitaxial growth of single-domain graphene on hexagonal boron nitride. *Nat. Mater.* **2013**, *12* (9), 792−797.
(10) El-Sherif, H.; Briggs, N.; Bersch, B.; Pan, M.; Hamidinejad, M.; Rajabpour, S.; Filleter, T.; Kim, K. W.; Robinson, J.; Bassim, N. D. Scalable characterization of 2D gallium-intercalated epitaxial graphene. *ACS Appl. Mater. Interfaces* **2021**, *13* (46), 55428−55439.
(11) Lin, J.; Peng, Z.; Liu, Y.; Ruiz-Zepeda, F.; Ye, R.; Samuel, E. L. G.; Yacaman, M. J.; Yakobson, B. I.; Tour, J. M. Laser-induced porous graphene films from commercial polymers. *Nat. Commun.* **2014**, *5* (1), 5714.
(12) Luo, Y.; Miao, Y.; Wang, H.; Dong, K.; Hou, L.; Xu, Y.; Chen, W.; Zhang, Y.; Zhang, Y.; Fan, W. Laser-induced janus graphene/poly(p-phenylene benzobisoxazole) fabrics with intrinsic flame retardancy as flexible sensors and breathable electrodes for fire-fighting field. *Nano Res.* **2023**, *16* (5), 7600−7608.
(13) Huang, L.; Liu, Y.; Li, G.; Song, Y.; Su, J.; Cheng, L.; Guo, W.; Zhao, G.; Shen, H.; Yan, Z.; Tang, B. Z.; Ye, R. Ultrasensitive, fast-responsive, directional airflow sensing by bioinspired suspended graphene fibers. *Nano Lett.* **2023**, *23* (2), 597−605.
(14) Yang, D.; Nam, H. K.; Le, T.-S. D.; Yeo, J.; Lee, Y.; Kim, Y.-R.; Kim, S.-W.; Choi, H.-J.; Shim, H. C.; Ryu, S.; Kwon, S.; Kim, Y.-J. Multimodal e-textile enabled by one-step maskless patterning of femtosecond-laser-induced graphene on nonwoven, knit, and woven textiles. *ACS Nano* **2023**, *17* (19), 18893−18904.
(15) Chu, G.; Zhang, Y.; Zhou, Z.; Zeng, W.; Chen, D.; Yu, S.; Wang, J.; Guo, Y.; Sun, X.; Li, M. Rapid CO_2-laser scribing fabrication of an electrochemical sensor for the direct detection of Pb^{2+} and Cd^{2+}. *Nano Res.* **2023**, *16* (5), 7671−7681.
(16) Yang, Y.; Song, Y.; Bo, X.; Min, J.; Pak, O. S.; Zhu, L.; Wang, M.; Tu, J.; Kogan, A.; Zhang, H.; Hsiai, T. K.; Li, Z.; Gao, W. A laser-engraved wearable sensor for sensitive detection of uric acid and tyrosine in sweat. *Nat. Biotechnol.* **2020**, *38* (2), 217−224.
(17) Su, R.; Liang, M.; Yuan, Y.; Huang, C.; Xing, W.; Bian, X.; Lian, Y.; Wang, B.; You, Z.; You, R. High-performance sensing platform based on morphology/lattice collaborative control of femtosecond-laser-induced MXene-composited graphene. *Adv. Sci.* **2024**, *11* (36), 2404889.
(18) Dosi, M.; Lau, I.; Zhuang, Y.; Simakov, D. S. A.; Fowler, M. W.; Pope, M. A. Ultrasensitive electrochemical methane sensors based on solid polymer electrolyte-infused laser-induced graphene. *ACS Appl. Mater. Interfaces* **2019**, *11* (6), 6166−6173.
(19) Chen, Y.; Xie, B.; Long, J.; Kuang, Y.; Chen, X.; Hou, M.; Gao, J.; Zhou, S.; Fan, B.; He, Y.; et al. Interfacial laser-induced graphene enabling high-performance liquid-solid triboelectric nanogenerator. *Adv. Mater.* **2021**, *33* (44), 2104290.
(20) Yang, W.; Han, M.; Liu, F.; Wang, D.; Gao, Y.; Wang, G.; Ding, X.; Luo, S. Structure-foldable and performance-tailorable PI paper-based triboelectric nanogenerators processed and controlled by laser-induced graphene. *Adv. Sci.* **2024**, *11* (28), 2310017.
(21) Ye, R.; James, D. K.; Tour, J. M. Laser-induced graphene: From discovery to translation. *Adv. Mater.* **2019**, *31* (1), No. e1803621.
(22) Peng, Z.; Ye, R.; Mann, J. A.; Zakhidov, D.; Li, Y.; Smalley, P. R.; Lin, J.; Tour, J. M. Flexible boron-doped laser-induced graphene microsupercapacitors. *ACS Nano* **2015**, *9* (6), 5868−5875.
(23) Le, T. S. D.; Lee, Y. A.; Nam, H. K.; Jang, K. Y.; Yang, D.; Kim, B.; Yim, K.; Kim, S. -W.; Yoon, H.; Kim, Y. -J. Green flexible graphene-inorganic-hybrid micro-supercapacitors made of fallen leaves enabled by ultrafast laser pulses. *Adv. Funct. Mater.* **2021**, *32* (20), 2107768.
(24) Lamberti, A.; Clerici, F.; Fontana, M.; Scaltrito, L. A highly stretchable supercapacitor using laser-induced graphene electrodes onto elastomeric substrate. *Adv. Energy Mater.* **2016**, *6* (10), 1600050.
(25) Pinheiro, T.; Morais, M.; Silvestre, S.; Carlos, E.; Coelho, J.; Almeida, H. V.; Barquinha, P.; Fortunato, E.; Martins, R. Direct laser writing: From materials synthesis and conversion to electronic device processing. *Adv. Mater.* **2024**, *36* (26), 2402014.
(26) Cheng, L.; Yeung, C. S.; Huang, L.; Ye, G.; Yan, J.; Li, W.; Yiu, C.; Chen, F.-R.; Shen, H.; Tang, B. Z.; et al. Flash healing of laser-induced graphene. *Nat. Commun.* **2024**, *15* (1), 2925.
(27) Wang, L.; Yin, K.; Li, X.; Huang, Y.; Xiao, J.; Pei, J.; Song, X.; Duan, J.-A.; Arnusch, C. J. Femtosecond laser ultrafast atomic scale renovating laser-induced graphene. *Adv. Funct. Mater.* **2025**, *35* (13), 2506215.
(28) Chen, P.; Yang, X.; Chang, Y.; Qian, W.; Fu, H.; Xu, W.; Ren, L.; Wang, Z.; Zu, H.; Wang, D.; et al. Superior microwave shielding modulation based on rapidly prepared graphene metasurface. *Natl. Sci. Rev.* **2025**, *12* (11), nwaf395.
(29) Vallés, C.; David Núñez, J.; Benito, A. M.; Maser, W. K. Flexible conductive graphene paper obtained by direct and gentle annealing of graphene oxide paper. *Carbon* **2012**, *50* (3), 835−844.
(30) Grimm, S.; Schweiger, M.; Eigler, S.; Zaumseil, J. High-quality reduced graphene oxide by CVD-assisted annealing. *J. Phys. Chem. C* **2016**, *120* (5), 3036−3041.
(31) Chen, P.; Li, N.; Chen, X.; Ong, W.-J.; Zhao, X. The rising star of 2D black phosphorus beyond graphene: Synthesis, properties and electronic applications. *2D Mater.* **2018**, *5* (1), 014002.
(32) Lv, Y.; Chen, P.; Foo, J. J.; Zhang, J.; Qian, W.; Chen, C.; Ong, W. J. Dimensionality-dependent MoS_2 toward efficient photocatalytic hydrogen evolution: From synthesis to modifications in doping, surface and heterojunction engineering. *Mater. Today Nano* **2022**, *18*, 100191.
(33) Su, M.; Chen, X.; Yang, L. CuO-embedded laser-induced graphene microfluidic system for continuous, non-invasive, and cost-effective glucose monitoring in sweat. *Chem. Eng. Sci.* **2025**, *314*, 121839.
(34) Wei, Y.; Li, W.; Zhang, S.; Yu, J.; Tang, Y.; Wu, J.; Yu, S. Laser-induced porous graphene/CuO composite for efficient interfacial solar steam generation. *Adv. Funct. Mater.* **2024**, *34* (28), 2401149.
(35) Ye, R.; Peng, Z.; Wang, T.; Xu, Y.; Zhang, J.; Li, Y.; Nilewski, L. G.; Lin, J.; Tour, J. M. In situ formation of metal oxide nanocrystals embedded in laser-induced graphene. *ACS Nano* **2015**, *9* (9), 9244−9251.
(36) Yang, L.; Yan, J.; Meng, C.; Dutta, A.; Chen, X.; Xue, Y.; Niu, G.; Wang, Y.; Du, S.; Zhou, P.; et al. Vanadium oxide-doped laser-induced graphene multi-parameter sensor to decouple soil nitrogen loss and temperature. *Adv. Mater.* **2023**, *35* (14), 2210322.
(37) Chen, P.; Ong, W.-J.; Shi, Z.; Zhao, X.; Li, N. Pb-based halide perovskites: Recent advances in photo(electro)catalytic applications and looking beyond. *Adv. Funct. Mater.* **2020**, *30* (30), 1909667.

(38) Li, Y.; Zeng, Z.; Zhang, S.; Yi, L.; Guo, D.; Zhao, Y.; Liu, F. Multifunctional metal-organic frameworks nanoengineered laser-induced graphene for health electronics. *Chem. Eng. J.* **2023**, *475*, 146330.
(39) Khandelwal, M.; Tran, C. V.; Lee, J.; In, J. B. Nitrogen and boron co-doped densified laser-induced graphene for supercapacitor applications. *Chem. Eng. J.* **2022**, *428*, 131119.
(40) Thompson, A. P.; Aktulga, H. M.; Berger, R.; Bolintineanu, D. S.; Brown, W. M.; Crozier, P. S.; In 't Veld, P. J.; Kohlmeyer, A.; Moore, S. G.; Nguyen, T. D.; et al. Lammps-a flexible simulation tool for particle-based materials modeling at the atomic, meso, and continuum scales. *Comput. Phys. Commun.* **2022**, *271*, 108171.
(41) Van Duin, A. C. T.; Dasgupta, S.; Lorant, F.; Goddard, W. A. Reaxff: A reactive force field for hydrocarbons. *J. Phys. Chem. A* **2001**, *105* (41), 9396−9409.
(42) Chenoweth, K.; van Duin, A. C. T.; Goddard, W. A. Reaxff reactive force field for molecular dynamics simulations of hydrocarbon oxidation. *J. Phys. Chem. A* **2008**, *112* (5), 1040−1053.
(43) Chen, Y.; Lu, X.; Ma, G.; Kim, M.; Yu, R.; Zhong, H.; Chan, Y. H. T.; Tan, M.; Liu, Y.; Li, M. G. One-step laser-guided fabrication of 3D self-assembled graphene micro-rolls. *ACS Nano* **2025**, *19* (5), 5769−5780.
(44) Chen, Y.; Guo, Y.; Xie, B.; Jin, F.; Ma, L.; Zhang, H.; Li, Y.; Chen, X.; Hou, M.; Gao, J.; et al. Lightweight and drift-free magnetically actuated millirobots via asymmetric laser-induced graphene. *Nat. Commun.* **2024**, *15* (1), 4334.
(45) Wang, Z.; Mao, B.; Zhao, M.; Calatayud, D. G.; Qian, W.; Li, P.; Hu, Z.; Fu, H.; Zhao, X.; Yan, S.; Kou, Z.; He, D. Ultrafast macroscopic assembly of high-strength graphene oxide membranes by implanting an interlaminar superhydrophilic aisle. *ACS Nano* **2022**, *16* (3), 3934−3942.
(46) Ferrari, A. C.; Meyer, J. C.; Scardaci, V.; Casiraghi, C.; Lazzeri, M.; Mauri, F.; Piscanec, S.; Jiang, D.; Novoselov, K. S.; Roth, S.; Geim, A. K. Raman spectrum of graphene and graphene layers. *Phys. Rev. Lett.* **2006**, *97* (18), 187401.
(47) Ferrari, A. C.; Basko, D. M. Raman spectroscopy as a versatile tool for studying the properties of graphene. *Nat. Nanotechnol.* **2013**, *8* (4), 235−246.
(48) Cao, S.; Fu, H.; Chen, P.; Feng, H.; Zhang, Z.; Lin, Z.; Wang, Z.; Qian, W.; Tian, C.; Li, L.; He, D. Weldable graphene foams for wide-range thermal switches. *Cell Rep. Phys. Sci.* **2025**, *6* (5), 102599.
(49) Cançado, L. G.; Takai, K.; Enoki, T.; Endo, M.; Kim, Y. A.; Mizusaki, H.; Jorio, A.; Coelho, L. N.; Magalhães-Paniago, R.; Pimenta, M. A. General equation for the determination of the crystallite size L_a of nanographite by Raman spectroscopy. *Appl. Phys. Lett.* **2006**, *88* (16), 163106.
(50) Yu, Y.; Qin, Z.; Zhang, X.; Chen, Y.; Qin, G.; Li, S. Far-from-equilibrium processing opens kinetic paths for engineering novel materials by breaking thermodynamic limits. *ACS Mater. Lett.* **2025**, *7* (1), 319−332.
(51) Xia, Z.; Huang, X.; Liu, J.; Dai, W.; Luo, L.; Jiang, Z.; Gong, S.; Zhao, Y.; Li, Z. Designing Ni_2MnSn heusler magnetic nanoprecipitate in copper alloy for increased strength and electromagnetic shielding. *Nat. Commun.* **2024**, *15* (1), 10494.
(52) Han, M.; Zhang, D.; Shuck, C. E.; McBride, B.; Zhang, T.; Wang, R.; Shevchuk, K.; Gogotsi, Y. Electrochemically modulated interaction of MXenes with microwaves. *Nat. Nanotechnol.* **2023**, *18* (4), 373−379.
(53) Zhou, X.; Min, P.; Liu, Y.; Jin, M.; Yu, Z.-Z.; Zhang, H.-B. Insulating electromagnetic-shielding silicone compound enables direct potting electronics. *Science* **2024**, *385* (6714), 1205−1210.
(54) Wang, R.; Ju, L.; Meng, X.; Yu, B.; Chen, H.; Li, S.; Fu, W.; Jiang, J.; Sun, Y.; Lu, W.; Dai, Y. Building thermal-conduction nanochannels in composite electromagnetic interference shielding film for electromagnetic heat management. *ACS Appl. Mater. Interfaces* **2025**, *17* (15), 23050−23061.
(55) Pan, F.; Shi, Y.; Yang, Y.; Guo, H.; Li, L.; Jiang, H.; Wang, X.; Zeng, Z.; Lu, W. Porifera-inspired lightweight, thin, wrinkle-resistance, and multifunctional MXene foam. *Adv. Mater.* **2024**, *36* (14), 2311135.
(56) Yang, S.; Lin, Z.; Wang, X.; Huang, J.; Yang, R.; Chen, Z.; Jia, Y.; Zeng, Z.; Cao, Z.; Zhu, H.; et al. Stretchable, transparent, and ultra-broadband terahertz shielding thin films based on wrinkled MXene architectures. *Nano Micro Lett.* **2024**, *16* (1), 165.

https://doi.org/10.1021/acsami.5c18748
ACS Appl. Mater. Interfaces 2025, 17, 64771−64782